Journal of the European Ceramic Society 45 (2025) 117674

Contents lists available at ScienceDirect

Journal of the European Ceramic Society

journal homepage: www.elsevier.com/locate/jeurceramsoc

Ultrafast sintering of 3D-printed 8YSZ for solid oxide fuel cells

Antonio Maria Asensio [a], Hauke Meier [a], Antonio Gianfranco Sabato [a], Ismael Babeli [a], Lourenço Martinho Serra [a], Santiago Márquez [a], Marc Nuñez [a], Marc Torrell [a], Albert Tarancón [a,b,*]

[a] Nanoionics and Fuel Cells, Catalonia Institute for Energy Research (IREC), Sant Adrià del Besòs, Barcelona 08930, Spain
[b] Catalan Institution for Research and Advanced Studies (ICREA), Passeig Lluís Companys 23, Barcelona 08010, Spain

ARTICLE INFO

Keywords:
Functional ceramics
Solid-state devices
Ultrafast High-temperature Sintering
3D-printing
Solid Oxide cells

ABSTRACT

Ceramic materials are key in energy technologies such as solid oxide cells or all-solid-state batteries. Recent advances in 3D-printing have pushed their potential, enabling unprecedented complex and customizable geometries. However, 3D-printing of ceramics involves remarkably long heat treatments, which limit their implementation. In this work, ultrafast high-temperature sintering was successfully employed to develop 3D-printed solid oxide electrolytes treated in less than 15 min, for the first time. The optimal sintering conditions resulted in > 96 % densification preserving structural integrity. Despite the presence of intragranular porosity, ascribed to the non-equilibrium conditions of the process, the final ionic conductivity remained within the expected range for 8YSZ. Additionally, the complete UHS 3D-printed electrolyte-supported cell demonstrated a peak power density exceeding 0.5 $W{\cdot}cm^{-2}$ at 900 °C, surpassing previously reported performances of similar systems. This highlights the potential of UHS as a final ceramic processing method to obtain highly densified and conductive materials with full functionality.

1. Introduction

In the new energy landscape, ceramic materials and devices are known to play a key role in efficient technologies that will boost the transition to a renewable energy scenario. Ceramic materials are used in a wide range of energy applications including solar panels, all solid-state batteries (ASSB), solid oxide cells (SOC), capacitors, thermoelectrics, thermoionics, thermal energy storage systems and piezoelectrics among others [1], due to their exceptional properties. Some of these properties include a wide range of electric and ionic conductivities, chemical stability and optical properties, which allow them to be used from room to high temperature applications. Although the inherent properties of ceramics are well understood, their fruitful exploitation relies not only on their chemistry, but also on the processing of the ceramic powder that tunes their properties through morphological key parameters which affect the mechanical, thermal, electrical and chemical response [2]. Specifically, in the energy sector parameters such as grain size and grain boundary morphology, porosity and tortuosity can be directly linked to their performance [3,4].

In the field of SOC, the cells manufacturing consists in subsequent deposition of flat layers of functional ceramics by screen-printing or tape casting followed by high temperature sintering thermal treatments. The overall workflow can include from two to four thermal treatments resulting in an expensive, time-consuming and energy intensive process [5]. Sintering of SOC state-of-the-art materials commonly requires high temperatures (i.e. >1350 °C [6,7]) to achieve the desired microstructure and densification of solid electrolytes and electrodes. Sintering is a fundamental process which leads to the transformation of compacted powder into densified pieces. This is achieved through atomic-scale transport mechanisms that couple particle bonding with porosity removal. In contrast, coarsening leads to grain growth while having a minimal impact on densification. The driving force for both processes is the energy minimization via chemical potential gradients arising from particle curvature (Eq. 1):

$$\Delta\mu = \quad \mu_{conv} - \mu_{conc} = \quad \gamma_{sv}{\cdot}\Omega{\cdot}\kappa \tag{1}$$

were μ_i stands for the chemical potential from the particles in contact, γ_{sv} is the interfacial energy, Ω is the volume of a formula unit and κ is the curvature. Based on this, the sintering mechanisms are associated with different diffusion mechanisms (D_i), including surface diffusion, volume diffusion and grain boundary diffusion, and the evaporation-

* Corresponding author at: Nanoionics and Fuel Cells, Catalonia Institute for Energy Research (IREC), Sant Adrià del Besòs, Barcelona 08930, Spain.
E-mail address: atarancon@irec.cat (A. Tarancón).

https://doi.org/10.1016/j.jeurceramsoc.2025.117674
Received 14 March 2025; Received in revised form 9 July 2025; Accepted 14 July 2025
Available online 16 July 2025

condensation phenomenon, all of them competing and leading to coarsening or densification [8] (Fig. S2). While surface diffusion and evaporation-condensation phenomena contribute to the coarsening of the particles, volume and grain boundary diffusion are the main mechanisms responsible for densification. All these diffusion mechanisms are thermally activated and follow an Arrhenius-type behavior:

$$D_i = A_0 \exp\left(-\frac{Q_i}{RT}\right) \quad (2)$$

where D_i is the diffusion coefficient, A_0 is the preexponential factor, Q_i the diffusion activation energy, R the gas constant and T for the temperature.

In practice, controlling the sintering conditions is essential to achieve the desired microstructure. Traditionally, the densification process of a green ceramic bodies (containing high amounts of organics) involves slow heating rates ($<1°C{\cdot}min^{-1}$) towards the sintering temperature where an hour-scale plateau is fixed. During this long process, the green ceramic body evolves from an initial 45–65 % relative density, through the gradual removal of organics, particle rearrangement and pore elimination, ultimately resulting in complete densification.

In the past significant efforts were made to optimize densification behavior by enhancing the diffusion processes, reducing sintering temperatures and shortening sintering time while preserving the desired microstructure. One of the earliest approaches involved using sintering aids, comprising additional compounds added to the material to facilitate the sintering process by promoting liquid-phase formation at low temperature, defect generation or grain boundary modification [9–11]. However, the use of metal oxides as sintering aids can alter properties such as electrical conductivity, phase stability and grain boundary conductivity, potentially leading to challenges for energy-related technologies where these properties are critical [12].

To address the energy-intensive and costly nature of traditional sintering processes while maintaining control over material chemistry, recent efforts have been focused on developing fast sintering methods [13,14]. As alternative strategies, current and magnetic field assisted sintering routes have emerged [15,16].

Flash sintering (FS), spark plasma sintering (SPS), including its pressure-less variants, microwave sintering (MWS) and ultrafast high-temperature sintering (UHS) are some of the most innovative approaches used in ceramic rapid sintering, each reducing the energy consumption and time required to achieve densification, through unique conditions and mechanisms [17–21]. Among the different approaches, UHS has recently emerged as a much more versatile technique that accelerates the sintering process, achieving significant sintering time reduction while producing highly densified ceramics. This sintering method is based on the Joule effect, allowing controlled temperature profiles by adjusting the current passing through the carbon felts. Temperatures as high as 3000 °C with rapid heating rates of 10^{3}-10^{4} $°C{\cdot}min^{-1}$ can be reached [13]. Additionally, unlike FS or MWS fast sintering techniques, UHS is not constrained by the polarity or conductivity of the material. This flexibility allows it to be applied across a broader range of materials without requiring complex instrumentation.

Focusing on the current state of UHS application to SOC electrolyte materials, several studies have been published concerning the use of UHS on 3 mol% yttria-stabilized zirconia (3YSZ) [15,20–22] but only one of them focused on the state-of-the-art material: 8 mol% yttria-stabilized zirconia (8YSZ) [22]. While 3YSZ is characterized by good high-temperature conductivity and strong mechanical properties, recent trends have aimed at reducing the operational temperature of SOCs. This shift has led to increased interest in more conductive electrolyte materials, such as 8YSZ which, despite demonstrating lower mechanical strength than 3YSZ, offers much higher ionic conductivity at lower temperatures. Specifically, 3YSZ has a fracture toughness of 5.8 $MPa{\cdot}m^{1/2}$ and an ionic conductivity of 0.038 $S{\cdot}cm^{-1}$ at 900 °C, while 8YSZ has a fracture toughness of 1.7 $MPa{\cdot}m^{1/2}$ and an ionic conductivity of 0.12 $S{\cdot}cm^{-1}$ at the same temperature [23].

With the increasing interest in optimizing electrolyte materials and accelerating their processing through advanced sintering techniques, parallel innovations in ceramics manufacturing are also gaining momentum. In particular, additive manufacturing (AM) has emerged as a transformative approach to fabricate SOC architectures with enhanced design flexibility. Among the different AM techniques used in ceramics, including direct inkjet wiring (DIW), binder jetting, selective laser sintering (SLS), stereolithography (SLA), digital light processing (DLP), fused filament fabrication (FFF) and robocasting (RC), SLA has gained attention as a particularly promising fabrication route, coupling high resolution printing and scalability [24–32]. In this regard, the authors lately demonstrated the significant potential of 3D printing fabricating highly performing SOC button cells [26,27], large-area cells [29] and, ultimately, as a complete 3D-printed stack [27].

Despite its inherent potential, 3D-printed complex-shaped ceramic pieces require thermal debinding processes which are characterized by even slower heating rates (0.1–1 °C/min) and multiple dwelling steps at temperatures between RT and 800 °C to ensure the safe and thorough removal of organic additives. This results in extremely long, energy-consuming and costly debinding and sintering thermal treatments that can last several days. This is particularly critical for techniques that involve a high volume of binders, where rapid heating can lead to cracks or internal stresses. Therefore, to facilitate the large-scale production and future mass deployment of SOC system based on 3D-printed electrolytes, disruptive solutions must be developed to drastically shorten processing time. Recent studies have demonstrated the potential of MW sintering, SPS and UHS in achieving highly densified 3D-printed ceramic parts [33–37]. UHS, in particular, has been applied to ceramic components fabricated by different additive manufacturing techniques, including FFF, DIW and DLP, with some reports indicating successful debinding and sintering [38,39]. However, these works typically involve materials with low binder content and do not address applications in SOC. To the best of the author's knowledge, the application of UHS to the complete processing of 3D-printed ceramic components for SOC has not yet been reported, making its demonstration with the state-of-the-art 8YSZ electrolyte particularly relevant and promising. Moreover, no prior work has included the electrochemical characterization of UHS sintered electrolytes in a complete cell configuration, which is essential to demonstrate their viability as a fully functional cell.

This work reports, for the first time, the complete thermal processing of 3D-printed 8YSZ electrolytes, comprising both debinding and sintering using UHS. The processed electrolytes were functionalized and electrochemically tested as complete SOC validating the proposed approach and demonstrating its potential as a future industrial ceramic processing method.

2. Experimental methods

2.1. Electrolytes fabrication

8 mol.% Y_2O_3-ZrO_2 (8YSZ) electrolytes were fabricated employing an industrial ceramic SLA 3D printer (Ceramaker C-900, 3DCeram Sinto). The commercial slurries (3DCeram Sinto) contained the ceramic 8YSZ powder dispersed in a UV-photocurable acrylate matrix with additives including a photoinitiator, plasticizers, dispersants and a vehicle. The slurry was spread onto the printing platform in 25 μm layers using a dual doctor blade system. Each layer was then selectively cured using a 355 nm UV laser with a power of 500 mW, a spot size of 40 μm and a scan speed of 550 $cm{\cdot}s^{-1}$. The laser parameters were adjusted to achieve a cure depth approximately four times the slice thickness, ensuring interlayer bonding. Computer aided design (CAD) model of the cell geometry (Figure S1) was sliced into 2D layers and sequentially printed along the z-axis. The green parts had an outer diameter of 2.5 cm and a total thickness of 250 μm. Additionally, a 3 mm wide ring was incorporated around the perimeter of the membranes to facilitate handling of

the printed components. Following the completion of printing, uncured slurry was removed using a commercial cleaning solution (Ceraclean, 3DCeram) and air blowing.

Thermogravimetric analysis (TGA) (TGA1, Mettler Toledo) was used to design an optimal debinding and sintering cycle of the printed parts and investigate the degradation temperatures of the organic components. The TGA measurements were performed under air atmosphere from 25 °C to 800 °C with a heating rate of 10 °C·min^{-1}. Based on the results and temperature profiles, the green 8YSZ bodies were heat treated employing an in-house built UHS system placed inside a glovebox to control the atmosphere. The system consists of a pair of carbon felts, within which the green ceramic body is embedded. Those felts are clamped by copper or steel plates connected to a power supply that pushes current through the felts increasing its temperature. The UHS setup, illustrated in Fig. 1, consisted of a carbon felt with the dimensions 10 cm× 4 cm x 0.5 cm (C-100, Fuel Cell Earth) clamped between four copper plates and connected to a power supply (PSI 9080–60 T, Elektro-Automatik). The green samples were inserted into a central slit made in the carbon felt. A type B thermocouple, connected to a data logger (TC-08, Picolog), was used to correlate current to temperature and ensure proper monitoring of the debinding and sintering temperature during the thermal processing. It is important to note that, although a thermocouple was used to monitor temperature, some discrepancies may arise as part of the heat is dissipated by the thermocouple tip, potentially leading to an underestimation of the actual temperature [40].

UHS processing comprised two steps: the debinding carried out in air and the sintering in argon, using stepwise current ramps with intermediate dwellings. Air was selected as the debinding atmosphere, as samples processed under argon were found to be more prone to delamination after sintering. Initially, for the debinding, a 10 A current was applied and maintained for 60 s, as preliminary tests indicated negligible impact on the sample due to minimal organic loss. Subsequently, the current was increased to 15 A at 0.1 A·s^{-1}, followed by a 60 s dwell. Given the increased sensitivity of the material at higher temperature, due to the high mass losses, the final ramp to 20 A was slowed to 0.05 A·s^{-1}, after which another 60 s dwell was applied. These stepped conditions were designed to gradually remove organics while minimizing structural degradation. As the final step, the sintering of the samples was carried out in argon atmosphere, which enabled higher temperatures while maintaining the integrity of the carbon felts. Two different sintering conditions were applied with final currents of 45 and 50 A, which approximately corresponded to 1450 °C and 1650 °C, respectively. The currents were initially adjusted to further test the densification level of the samples but also to establish a comparison with conventional sintering temperature of 8YSZ, which typically ranges between 1350 and 1450 °C.

For comparison purposes, additional 3D printed 8YSZ samples were processed using conventional thermal treatment, as explained elsewhere [26,41], with a final sintering temperature of 1450 °C.

2.2. Cells functionalization

Symmetrical cells, Pt|8YSZ|Pt, were initially fabricated to measure the ionic conductivity of the printed electrolytes. To do so, platinum was painted on each side of the 8YSZ and cured at 1000 °C for 30 mins.

For the preparation of the complete cells, different steps were followed. First, to prevent the formation of isolating zirconates phases during the sintering of the oxygen electrode caused by the cationic interdiffusion and reaction between lanthanum and strontium with the zirconium from the YSZ electrolyte, a GDC barrier layer was deposited using a large-area pulsed laser deposition (PLD) system (PVD500, PVDproducts). A total of 36.000 pulses was used, resulting in a film approximately 300 nm thick, deposited at 600 °C. Further details on the deposition process can be found in our previous publications [42,43]. After GDC deposition the electrolytes were functionalized with self-formulated inks for both, fuel and oxygen electrodes. The electrode inks were prepared by using commercial NiO-YSZ powders for the fuel electrode and $La_{0.6}Sr_{0.6}Co_{0.2}Fe_{0.8}O_3$ - $Ce_{0.8}Gd_{0.2}O_{2-\delta}$ (LSCF-CGO) for the oxygen electrode (both from FuelCellMaterials), with terpineol (Sigma Aldrich) used as vehicle with a 1:2 wt ratio. The electrode deposition was carried out by slurry coating. The sintering of the electrodes was perfomed in a two-step process: the first sintering at 1400 °C for 2 h and the second at 1050 °C for 2 h, for the fuel and oxygen electrodes, as already optimized in previous works [6,44].

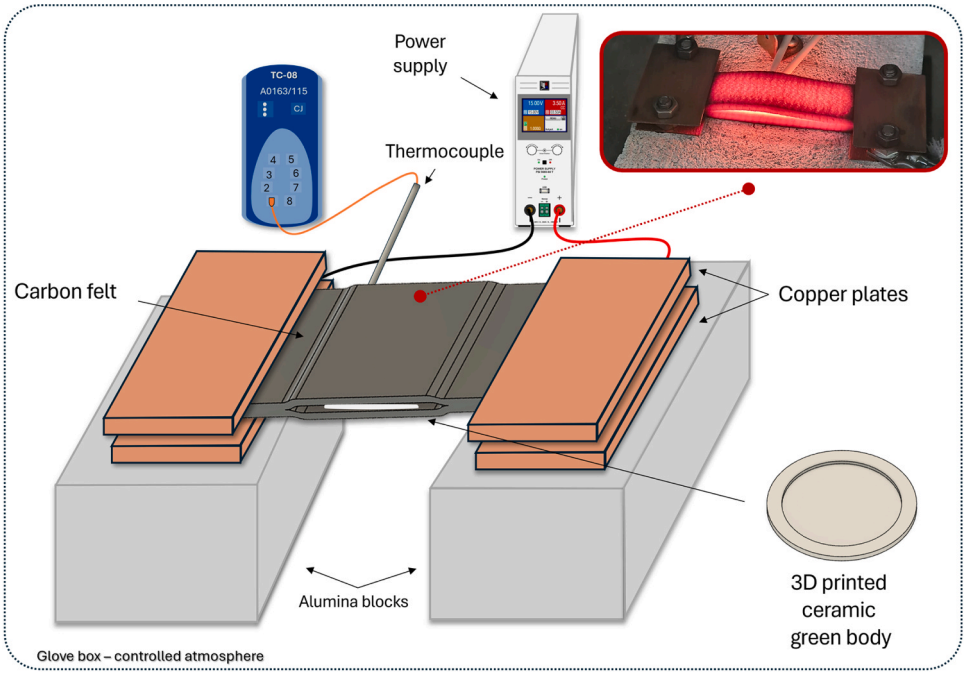

Fig. 1. Schematic representation of the UHS setup for sintering, including: the heating elements, the power supply and the elements for temperature monitoring (inset: Close-up photograph of the UHS under operation).

2.3. Electrochemical, structural and morphological characterization

The symmetrical cells with the configuration Pt|8YSZ|Pt were characterized by electrochemical impedance spectroscopy (EIS) in the 300 – 900 °C range under air atmosphere by using a frequency response analyzer (Parstat 2273, Princeton Applied Research). The collected Nyquist plots were fitted by Zview software to assess the contribution of bulk and grain boundaries to the total ionic resistance for each temperature and, consequently, calculate the conductivity.

The electrochemical characterization of the complete button cells with the configuration LSCF-CGO|CGO|8YSZ|NiO-YSZ was performed by employing *i*-V polarization curves and EIS. The sealing of the complete cells was done by using a high-temperature adhesive (Ceramabond 552, Aremco). Gold and nickel meshes and wires were used to assemble the electrical connection. The characterization was performed under SOFC in the 750 – 900 °C temperature range. During SOFC operation, the oxygen electrode was fed with 125 mL·min^{-1} of air while the fuel electrode was fed with 50 mL·min^{-1} of dry H_2 by using a gas-flow controller (Bronkhorst). Both symmetrical and complete cells were characterized in commercial Probostat (NorECS) test-benches.

The crystal structure of the sintered materials was assessed by X-ray diffractometry (XRD, Bruker D8 ADVANCE) with Cu Kα radiation (λ = 1.5406 Å). The XRD patterns were collected in the 2θ range of 20–90 ° with a step size of 0.02 ° and an integration time of 1 s. The morphological and microstructural characterization of the cross-sections of the fractured samples was imaged by scanning electron microscopy (SEM, AURIGA Gemini 30 kV FESEM, ZEISS). Relative density was determined using the Archimedes method with water as the immersion medium. Samples were weighed in air and then submerged in deionized water at room temperature (~25 °C) to obtain the apparent weight in liquid. The theoretical density of 8YSZ was considered as 5.98 g·cm^{-3}. Grain size measurements were performed by analyzing a hundred individual grains from SEM micrographs

3. Results

3.1. Fabrication, characterization and processing of 8YSZ 3D-printed membranes

SLA 3D printing was employed to produce 8YSZ button cells with a diameter of 2.5 cm, comprising a 3 mm support ring and a thin electrolyte membrane, approximately 250 μm in thickness. Prior to thermally processing the as-printed green membranes, TGA analyses were performed with the aim of understanding the critical steps on the debinding and sintering of the printed parts and, consequently, design an optimal debinding and sintering cycle to be applied during both, conventional and UHS sintering processes. Fig. 2 presents the TGA profile, and its first derivative recorded for the green 8YSZ cured pieces obtained after the 3D printing. The total weight loss reached 15.4 wt%, divided into three distinct temperature ranges with weight loss steps of 0.8, 12.0, and 2.6 wt%, respectively. The derivative TGA curve highlights key decomposition temperatures within this critical region. The peak at 192 °C reflects the initial decomposition of the organic solvent, the most volatile compound in the slurry which acts as the vehicle. This is followed by a prominent weight loss step of 12 wt% with a maximum peak at 340 °C, attributed to the decomposition of the monomer used in the printing slurry. Finally, a lower weight loss of 2.4 wt% corresponds to the decomposition of residual additives. No weight changes are observed beyond 450 °C, indicating the completion of the debinding process.

To achieve fully sintered 3D-printed green bodies, the thermal profile applied by UHS was designed based on the presented results from the TGA analysis, ensuring the full decomposition of the organics at each step. This is particularly critical in the debinding step, where a swift temperature increase results in excessive CO_2 release, leading to severe cracking and deformation of the printed parts, as previously reported by

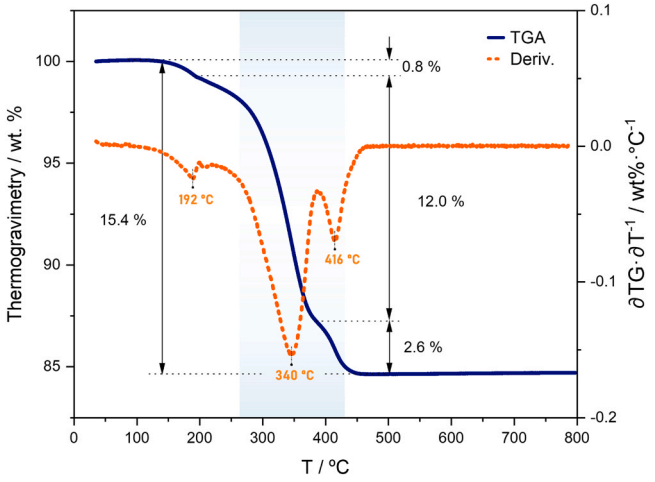

Fig. 2. TGA and its first derivative showing weight loss and corresponding decomposition rates of the as-printed 8YSZ green parts. The critical temperature stage, comprising the maximum peak decomposition rates at approximately 340 °C and 416 °C, is highlighted in blue.

Bhandari et al. [34]. In order to select the different applied currents and dwelling steps, which would correspond to the points in which the decomposition of the organics occurs, a prior optimization was conducted correlating current, dwelling times and temperature. Fig. 3 shows the optimized thermal profiles, along with its corresponding electrical profile, used for the UHS processing during the debinding and sintering, as shown in Fig. 3a and b, respectively. The critical temperature stage of the debinding process, deduced by the TGA analysis, is also highlighted in blue.

The applied three-steps debinding process, using 10 A, 15 A and 20 A for 60 s each, ensured a gradual release of both CO_2 and H_2O formed during the decomposition of the organics. A final step at 20 A for 60 s, corresponding to approximately 500 °C, was added to the sequence to ensure that the organic matter decomposition at lower temperatures was completed, before heat treating the samples in the subsequent sintering process. To further investigate the densification behavior and microstructural evolution of 8YSZ membranes, two distinct final sintering temperatures were chosen for the UHS processed samples: achieved by applying 45 A and 50 A for 60 s of dwelling. The first treatment, corresponding to 45 A, was chosen to reach 1450 °C, corresponding to the conventional sintering temperature used for 8YSZ. Conventional sintering of 8YSZ using furnaces typically [7,45] involves slow heating ramps with 1–2 °C·min^{-1} and long dwelling times ≥ 2 h. at 1350–1500 °C to ensure controlled densification without excessive grain growth or microstructural degradation led by coarsening, being both processes highly influenced by temperature, (Fig. S2). By applying 50 A, the second sample was sintered at 1650 °C, as presented in Fig. 3b, while keeping the same debinding procedure. The choice of this higher temperature was motivated by the nature of sintering process, where the rapid heating rates and shorter dwelling times are expected to mitigate some of the drawbacks traditionally associated with long dwelling times at high temperature, such as uncontrolled grain growth, thermal degradation leading to undesired phases, excessive coarsening or even material losses due to evaporation [30,31].

Fig. 4 compares the phase composition and physical appearance of 3D printed 8YSZ samples before and after sintering under UHS and conventional conditions. The XRD patterns, Fig. 4(a), with specified diffraction peaks assigned to the PDF n# 01–070–4431, confirm that the sintering procedure does not affect the final single cubic phase of 8YSZ. The optical images in Fig. 4(b) show the physical appearance of the samples in the green state and after sintering, illustrating the shrinkage and densification associated with thermal treatment. Minimal shrinkage is observed for the UHS-1450, while samples sintered at 1650 °C via

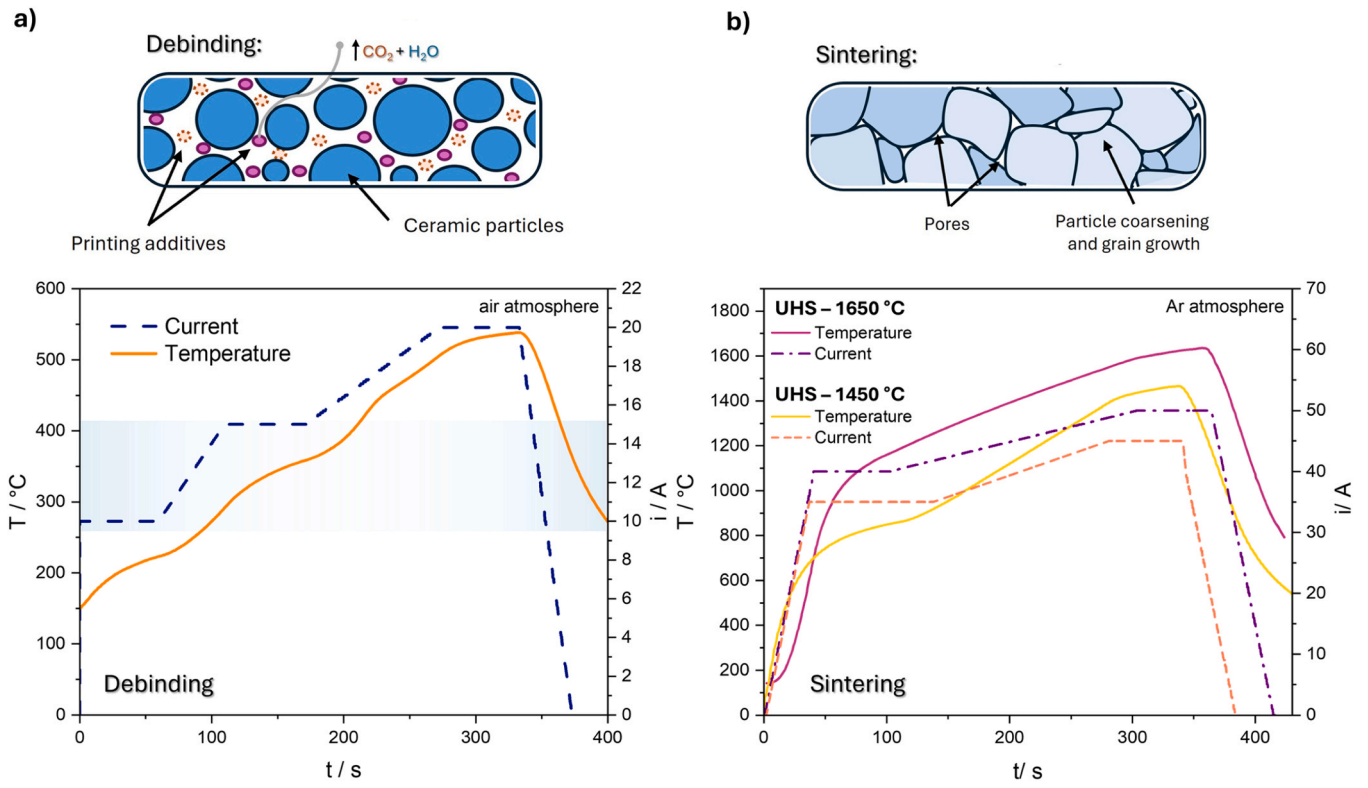

Fig. 3. UHS heat treatment and corresponding electrical profile applied to the as-printed 8YSZ membranes for (a) debinding and (b) sintering for both UHS-treated conditions.

UHS and by the conventional route show comparable final dimensions, indicating similar levels of densification. A slight color change was observed at the outer ring of the sample sintered at the highest temperature (see Fig. S3), however this had no impact on the phase composition or on the material's conductivity, as will be discussed later.

In Fig. 5(a-f) the SEM micrographs of both conventional and UHS treated samples are presented. High densification (>96 %) were achieved for both, the conventional treated sample Fig. 5(a,b), and the UHS-treated sample sintered at the highest temperature, corresponding to 1650 °C, Fig. 5(e,f). In contrast, the UHS-treated sample sintered at 1450 °C, matching the temperature of the conventional treatment, exhibited lower densification (~82 %), as presented in Fig. 5(c,d). This sample showed significantly finer grains and increased porosity, suggesting that the shorter dwelling time at this temperature was insufficient to complete densification.

While both, conventionally treated and UHS-1650 samples show high densification with good grain connectivity, the differences in porosity between them are notable (Fig. 5b,f). The conventionally sintered sample exhibits slightly smaller grain size with a narrow distribution (0.81 ± 0.18 μm), and minimal porosity is mostly located at the grain boundary (solid arrow). In contrast, the UHS-treated sample exhibits a larger grain size with with a broader distribution (1.4 ± 0.37 μm). This broader distribution may be attributed to the UHS process, where the outer regions of the sample are more exposed to the felt temperature, creating a gradient of temperature resulting in grain size variation. In addition to porosity at the grain boundaries, the UHS-treated sample also exhibits intragranular porosity (dashed arrows). This type of intragranular porosity is likely due to the high grain booundary mobility associated with the rapid heating rates, which can lead to grain growth that outspaces pore elimination, resulting in pore entrapment.

Based on previous studies focused on the microstructural characteristics derived from ultrafast sintering processes [46,47], some conclusions about the underlying sintering mechanisms linked to our results can be made. While a contribution from the higher sintering temperature in the UHS process is expected, it is evident that the rapid heating rate plays an important role in enhancing the densification. The initial heating rate surpasses the regime when most coarsening occurs, leading to increased grain boundary mobility and volume diffusion, both of which are enhanced at high temperatures and influence pore removal and densification, Fig. S2c. However, the combination of high heating rates and short dwelling times, can lead to a mismatch between grain growth and pore elimination. In particular, the rapid migration of grain boundaries may outpace the redistribution and pore removal, resulting in the pore entrapment within growing grains [46,48].

To investigate how the observed microstructural features influence ionic transport, electrochemical impedance spectroscopy was conducted in symmetrical cell configuration using platinum contacts (Pt|8YSZ|Pt). The results as Nyquist plots for 400 °C and 500 °C are reported in Fig. 6 (a,b) and the individual contributions of the bulk (R_{bulk}) and grain resistance (R_{GB}) are reported in Fig. 6(c,d) as Arrhenius plots, for the 400 – 500 °C temperature range. For the deconvolution of the individual contributions, simple equivalent circuits models based on primary electric components (L = inductance, R = resistance and Q = constant phase element) were used. From the Nyquist plots shown in Fig. 6(a) and (b) it can be observed that the primary difference in between the conventionally sintered sample with respect to the one treated by UHS at 1650 °C, is concentrated in the bulk resistance (R_{bulk}) mainly attributed to the presence of intragranular porosity. As the temperature is further increased, Fig. 6(b), the specific resistance of the bulk is shifted towards higher frequencies, allowing a clearer comparison of the grain boundary (R_{GB}) contribution. In Fig. 6 (b), it can be noticed that the R_{GB} behavior from both samples is similar, with R_{GB} values being 6.6 Ω·cm^2 for the conventional sample and 9.5 Ω·cm^2 for the UHS-1650 sample. The slightly higher resistive behavior for the UHS sample is assigned to the higher porosity at the grain boundary.

Building upon the impedance results, the extracted values of R_{bulk} and R_{GB} were analyzed across temperature in the form of Arrhenius plots

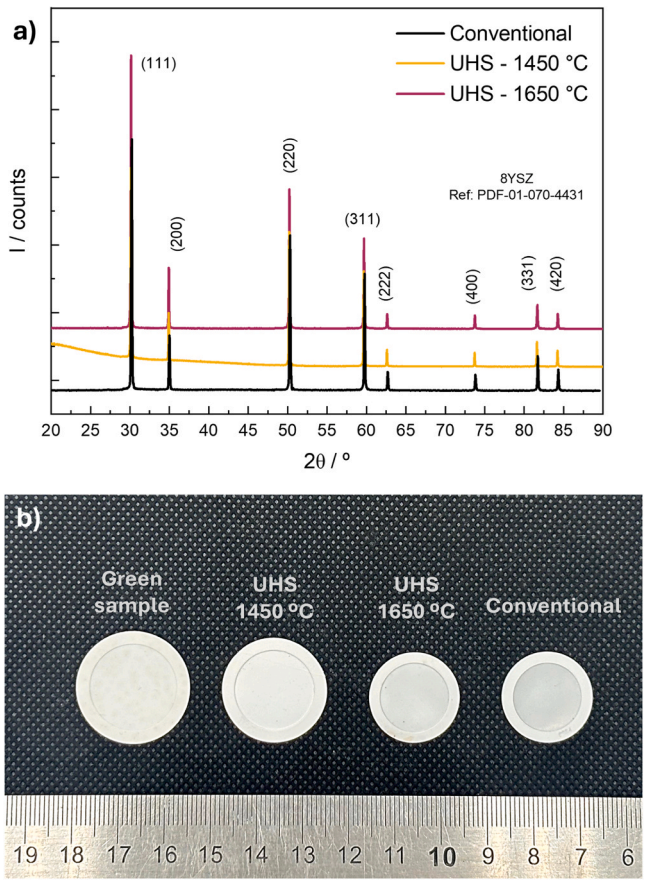

Fig. 4. a) XRD diffractogram showing the diffraction peaks corresponding to the single cubic phase of 8YSZ for the as treated samples under conventional and UHS sintering conditions; b) Optical images showing the resulting 8YSZ samples in the green state and processed under different sintering conditions.

Fig. 6(c,d). These plots further confirm that, despite differences in microstructure and porosity, the activation energies for bulk conductivitiy remain consistent across the samples: 1.04 eV for conventional and UHS-1650, and 1.06 eV for UHS-1450. This reinforces that bulk conductivity is primarly governed by the instrinsic concentration and mobility of oxygen vacancies introduced by the Y^{3+} doping, and is therefore minimally affected by sintering-induced microstructural variations, such as porosity or grain size, as long as the phase composition and dopant levels remains unchanged [49].

In contrast, grain boundary conductivity shows a more pronounced variation between samples, particularly for the lower temperature UHS-1450 condition. Although the grain boundary activation energy remains in the range (1.11–1.14 eV), the absolute values of conductivity differ noticeably. As seen in Fig. 6d, the UHS-1450 sample shows a markedly higher grain boundary resistance (R_{GB} 162 Ω·cm^2 vs 12.7 Ω·cm^2 for the conventional at 500 °C). This is attributed to its limited grain growth and higher boundary volume fraction, as supported by the morphological analysis in Fig. 5.

Total conductivity (σ_{Total}) is presented in Fig. 7. At 750 °C, the σ_{Total} values are comparable for the UHS-1650 and conventionally treated samples with 0.021 S·cm^{-1} and 0.030 S·cm^{-1}, respectively. In contrast, UHS-1450 exhibits a significantly lower conductivity, 0.006 S·cm^{-1}. In addition to this overall lower conductivity, the UHS-1450 sample shows a slight deviation from linear Arrhenius behavior, which may indicate a change in the dominant transport mechanism or defect structure at intermediate temperatures. A possible explanation may be attributed to the formation of oxygen vacancy clusters, a characteristic phenomenon in doped zirconia-based systems. As reported in the literature, the formation of these clusters occurs when dopant ions act as nucleation centers for the condensation of oxygen vacancies reducing ionic mobility and consequently decreasing conductivity [50]. This effect becomes more pronounced when sintering is performed at lower temperatures, as in the case of UHS-1450, where the lower solubility of vacancies in the crystalline matrix may explain the observed decrease in conductivity. In contrast, the activation energy remains almost unchanged for all the sintering conditions, 0.99–1.01 eV. Despite, differences among samples, all the conductivities fall within the literature values reported for 8YSZ produced via conventional shaping processes (not 3D printed) [26,51–53]. Weber et al. studied the different conductivity for a wide range of materials under conventional processing, reaching a conductivity of 0.09 S·cm^{-1} at 900 °C on 8YSZ. Notably, for 3D-printed 8YSZ, the values previously published were nearly identical [26]. Pesce et al. also reported an overall conductivity of 0.06 S·cm^{-1} at 900 °C for a 3D-printed 8YSZ. This confirms that there is no detrimental effect on the ionic conductivity of 8YSZ process by rapid debinding and sintering using UHS.

Based on the results obtained in symmetrical cell configuration, a

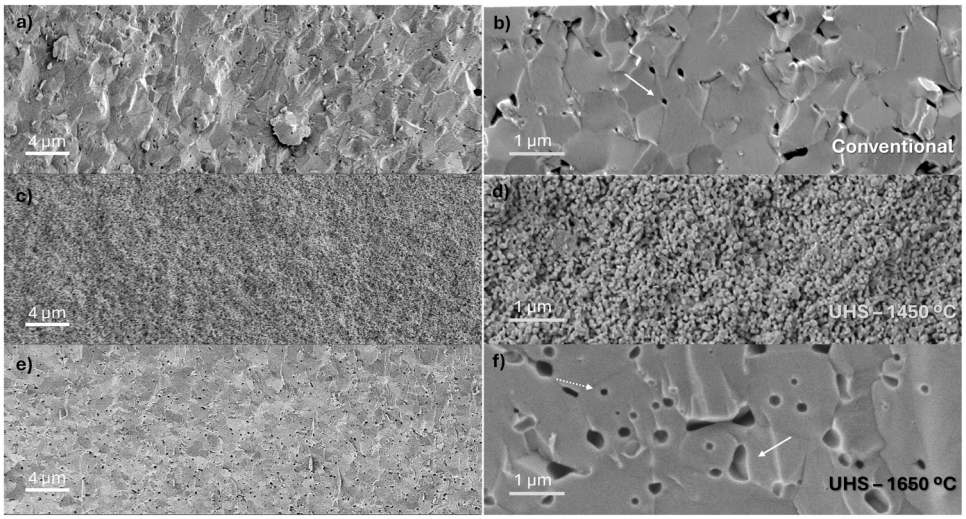

Fig. 5. SEM cross sectional micrographs at different magnification of the symmetrical cells heat treated under (a,b) conventional conditions, (b,c) UHS at 1450 °C and (e,f) UHS at 1650 °C. The different arrows indicate the two types of porosity present in the UHS-treated sample: solid arrows point to porosity at the grain boundaries while dashed arrows point to intragranular porosity.

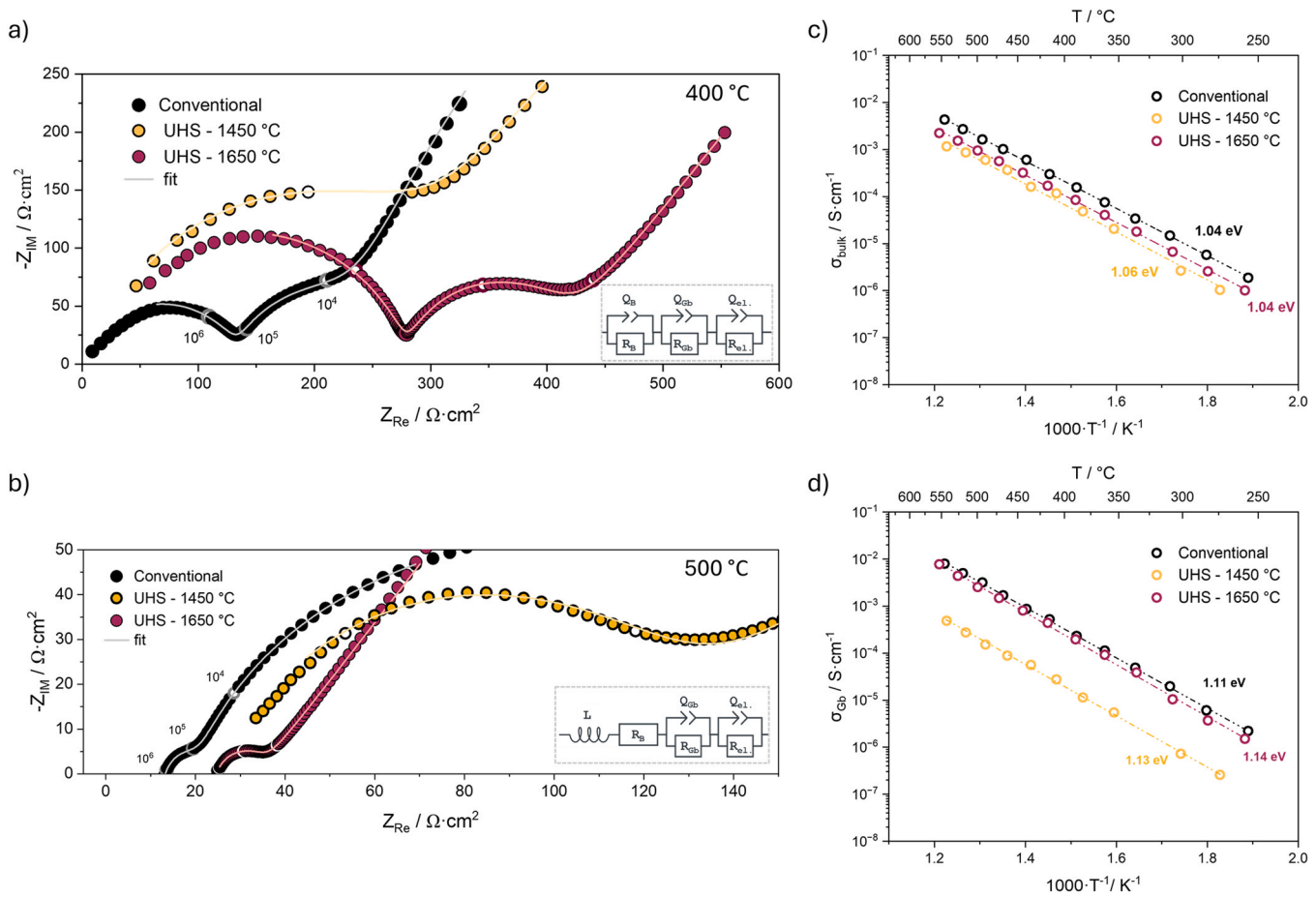

Fig. 6. EIS results of symmetric Pt/8YSZ/Pt cells: (a, b) Nyquist plots with the equivalent circuit used for data fitting shown in the insets at 400 °C and 500 °C, respectively, with the corresponding frequency decades indicated; (c, d) Arrhenius plots displaying the individual resistive contributions (R_{bulk} and R_{gb}) within the 250–600 °C temperature range, measured under air by both UHS and conventional heat treatments.

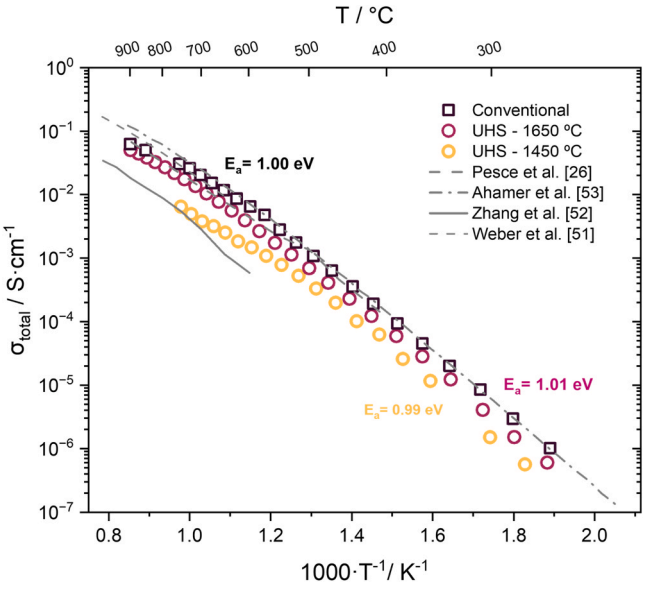

Fig. 7. Arrhenius plot of the total conductivity for UHS-sintered and conventionally treated samples under symmetrical cell configuration Pt/8YSZ/Pt, measured in air over the 250 – 900 °C temperature range, compared to data from the literature [26,51–53].

complete cell was fabricated using the best conditions. The 3D printed electrolyte was debinded and sintered by UHS at 1650 °C. A complete cell with the configuration LSCF-CGO|CGO_{PLD}|$8YSZ_{UHS-1650}$|NiO-YSZ and fabricated as discussed in the experimental section was electrochemically tested. Its corresponding cross-sectional SEM micrographs after measurements are shown in the Fig. 8 panel.

From the SEM micrographs it can be observed that a 200 μm-thick 8YSZ membrane was achieved (Fig. 8a). A detailed micrograph of the 8YSZ membrane is shown in Fig. 8c, confirming an almost fully densified structure characterized by two types of porosity as previously discussed. A slightly denser region (~20 μm) near the top and bottom surfaces can be observed, which is consistent with earlier observations in the symmetrical cells (UHS-1650, Fig. 5e) and likely results from the thermal gradient during UHS, where outer surfaces are more exposed to heat. Additionally, both electrodes, LSCF-CGO and NiO-YSZ shown in Fig. 8b and d, presented good homogeneity and adhesion characterized with a highly interconnected interface and adequate porosity.

The *i-V* and *i-P* curves as well as the Nyquist plots of the complete cell are shown in Fig. 9. The cell exhibited a maximum current density of almost 1 $A{\cdot}cm^{-2}$ at 0.6 V with a peak power density above 0.5 $W{\cdot}cm^{-2}$ at 900 °C, as shown in Fig. 9a. This is a remarkable power output considering the relatively thick electrolyte (~200 μm) obtained by 3D printing. Additionally, the gas tightness of the 8YSZ membrane is validated by the recorded open circuit voltage (OCV), reaching values above 1.15 V. This result demonstrates the suitability of the sintering process to produce fully densified crack-free electrolytes.

In Fig. 9b the Nyquist plots of the complete cell measured at OCV are shown. The inset reveals that at 900 °C low ohmic losses are measured,

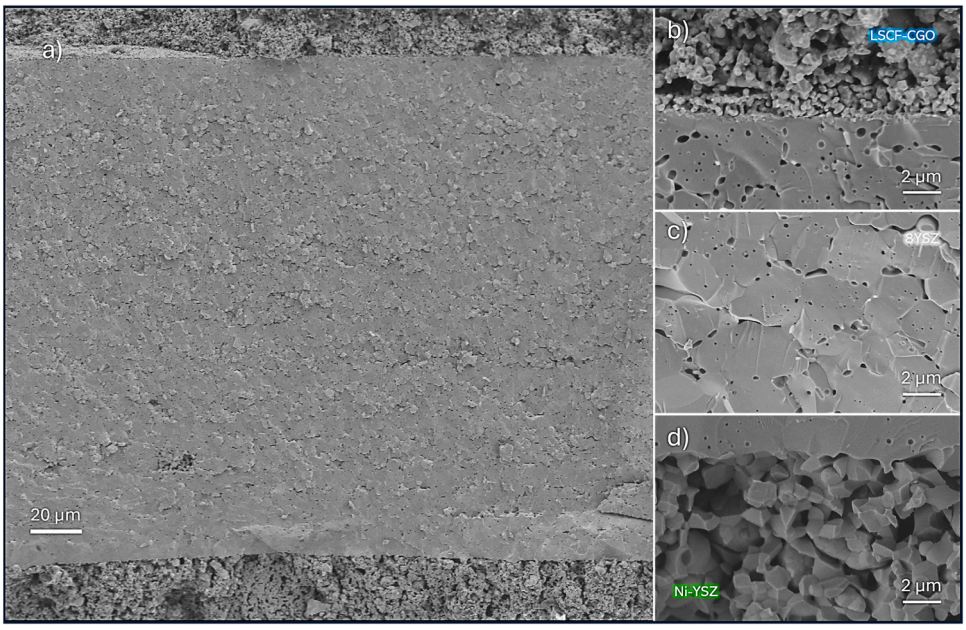

Fig. 8. SEM cross section micrographs showing the structural details of the complete cell: (a) cross-sectional overview of the cell showing all the layers LSCF-CGO|CGO_{PLD}|$8YSZ_{UHS\text{-}1650}$|NiO-YSZ; (b) 8YSZ membrane (c) oxygen electrode-electrolyte interface and (d) fuel electrode-electrolyte interface.

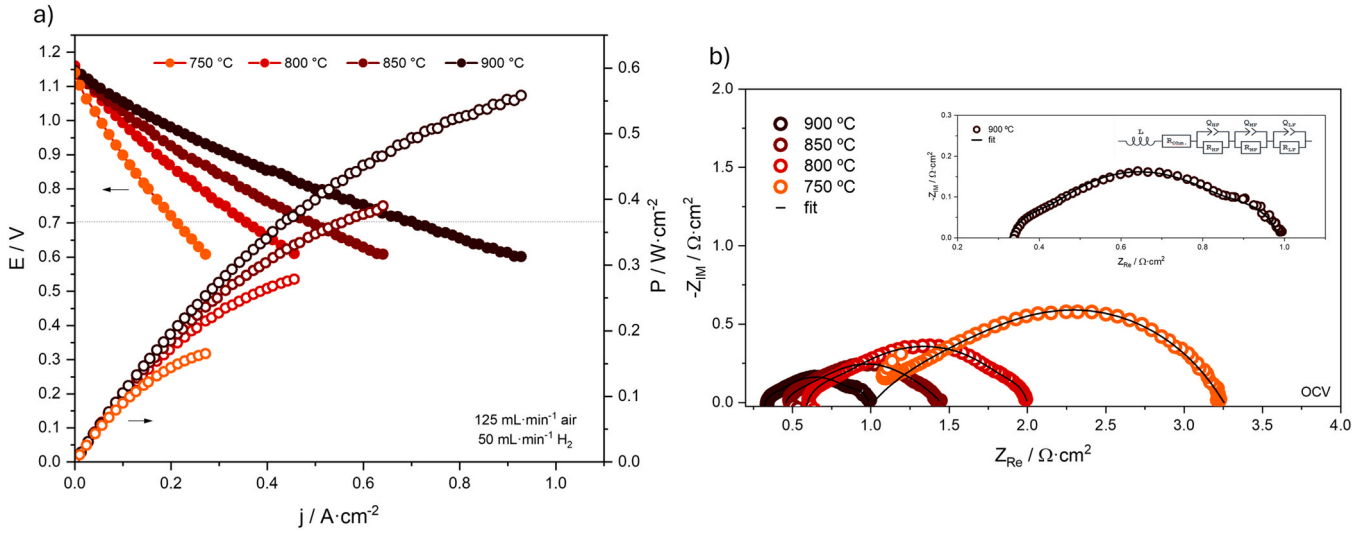

Fig. 9. (a) i-V and i-P curves for the LSCF-CGO|CGO_{PLD}|$8YSZ_{UHS\text{-}1650}$|NiO-YSZ cell in the 750–900 °C temperature range in SOFC conditions; (b) Nyquist plots and fitting at OCV (used equivalent circuit on the inset).

reaching 0.33 Ω·cm^2, which corresponds to 0.058 S·cm^{-1} (Fig. S4). This value is slightly higher than the conductivity achieved in symmetrical cell measurements, probably due to some contribution on the contact resistance of the electrodes, and close to the conventional sintering sample (Fig. 7).

When compared to similar 3D printed complete cells sintered by conventional treatment and reported in literature [26,41], the achieved performance is notably higher than previous publications. Márquez et al. reached ~0.5 A·cm^{-2} at 0.6 V employing 3D printed YbScSZ electrolytes (265 µm thick) at 900 °C with the identical design used in the present paper (flat button cell). Similarly, Pesce et al. reached ~0.4 A·cm^{-2} at 0.6 V for a 3D printed 8YSZ electrolyte (270 µm thick) by using LSM-YSZ as oxygen electrode. The observed high performance of the here developed SOFC can be attributed primarily to the full densification of the 8YSZ membrane.

4. Conclusions

This work demonstrated the suitability of Ultrafast High-temperature Sintering (UHS) for fabricating 3D printed SOC electrolytes substituting energy- and time-consuming debinding and sintering conventional thermal treatments. The UHS approach significantly reduced the overall processing time for debinding and sintering of 3D printed 8 mol.% Yttria Stabilized Zirconia from days to less than 15 min. 3D printed 8YSZ membranes sintered by UHS at 1650 °C reached high levels of densification (>96 %), proved to be crack-free and demonstrated their functionality as electrolytes for SOC applications with an ionic conductivity of 0.05 S cm^{-1} at 900 °C. In the morphological study carried out, it was concluded that the non-equilibrium conditions generated by such fast-heating rates lead to permanent intragranular porosity. A slight decrease in bulk conductivity was observed, without excessively impacting the total conductivity under operating conditions.

The measured conductivity remained consistent with values reported in literature for 8YSZ (including those from 3D printed electrolytes thermally treated in conventional sintering).

Using 3D printed and UHS-sintered 8YSZ electrolytes, full solid oxide fuel cells were successfully fabricated (LSCF-CGO|CGO_{PLD}|$8YSZ_{UHS-1650}$|NiO-YSZ) exhibiting a maximum current density of almost 1 $A{\cdot}cm^{-2}$ at 0.6 V, with a peak power density above 0.5 $W{\cdot}cm^{-2}$, at 900 °C. This excellent performance highlights the effectiveness of UHS in producing fully functional 8YSZ electrolytes. The achieved performance aligns with the expectations considering the employed materials (especially an electrolyte thickness of 200 μm) outperforming previously reported cells using conventionally treated 3D printed electrolytes.

These results open a new avenue for the fabrication of complex-shaped solid oxide cells by combining 3D printing and UHS as advanced processing methods, which could represent a breakthrough in the field of ceramics for energy applications in terms of time, cost and energy consumption compared to conventional processing.

CRediT authorship contribution statement

Marc Torrell: Writing – review & editing, Supervision, Conceptualization. **Albert Tarancón:** Writing – review & editing, Supervision, Conceptualization. **Antonio Maria Asensio:** Writing – review & editing, Writing – original draft, Visualization, Investigation, Formal analysis, Data curation. **Hauke Meier:** Writing – review & editing, Investigation. **Lourenço Martinho Serra:** Writing – review & editing, Investigation. **Santiago Márquez:** Writing – review & editing, Investigation. **Antonio Gianfranco Sabato:** Writing – review & editing, Resources, Investigation. **Ismael Babeli:** Writing – review & editing, Investigation. **Marc Nuñez:** Writing – review & editing, Resources, Investigation.

Declaration of Competing Interest

The authors declare that they have no known competing financial interests or personal relationships that could have appeared to influence the work reported in this paper.

Acknowledgements

The authors gratefully acknowledge the funding from the European Union through the CleanHyPro project (Gant Agreement No. 101091777). This work is also part of the research activities of Hy-Spire project (Gant Agreement No. 101137866) supported by the Clean Hydrogen Partnership. The authors also acknowledge support from the Spanish Government (PID2022–136883OB-C22, Fassion3D) and Generalitat de Catalunya (2021-SGR-00750, NANOEN). Dr. A. Maria Asensio would like to acknowledge Juan de la Cierva fellowship (JDC2023–052569-I, funded by MCIU/AEI/10.13039/501100011033 and by FSE+). Dr. A.G. Sabato would like to acknowledge Ramon y Cajal fellowship (RYC2021–034470-I, funded by MCIU/AEI/10.13039/501100011033 and by European Union NextGenerationEU»/PRTR).

Appendix A. Supporting information

Supplementary data associated with this article can be found in the online version at doi:10.1016/j.jeurceramsoc.2025.117674.

References

[1] O. Guillon. Advanced Ceramics for Energy Conversion and Storage, Elsevier/The Lancet, 2019.
[2] M.N. Rahaman. Ceramic Processing, 2 ed., CRC press, 2017.
[3] O. Guillon, Ceramic materials for energy conversion and storage: a perspective, Int. J. Ceram. Eng. Sci. 3 (3) (2021) 100–104.
[4] K.S. Randhawa, Advanced ceramics in energy storage applications: batteries to hydrogen energy, J. Energy Storage 98 (2024) 113122.
[5] M.R. Weimar, L.A. Chick, D.W. Gotthold, G.A. Whyatt, Cost Study for Manufacturing of Solid Oxide Fuel Cell Power Systems, United States, 2013.
[6] M. Irshad, M. Rafique, A.N. Tabish, A. Ghaffar, A. Shakeel, K. Siraj, Qu Ain, R. Raza, M.A. Assiri, M. Imran, Influence of sintering temperature on the structural, morphological, and electrochemical properties of NiO-YSZ anode synthesized by the autocombustion route, Metals 12 (2) (2022) 219.
[7] I.R. Gibson, G.P. Dransfield, J.T.S. Irvine, Sinterability of commercial 8 mol% yttria-stabilized zirconia powders and the effect of sintered density on the ionic conductivity, J. Mater. Sci. 33 (17) (1998) 4297–4305.
[8] M. Barsoum. Fundamentals of Ceramics, 2 ed., Taylor & Francis, London, England, 2022.
[9] J. Hostaša, F. Picelli, S. Hříbalová, V. Nečina, Sintering aids, their role and behaviour in the production of transparent ceramics, Open Ceram. 7 (2021) 100137.
[10] P. Babilo, S.M. Haile, Enhanced sintering of Yttrium-doped barium zirconate by addition of ZnO, J. Am. Ceram. Soc. 88 (9) (2005) 2362–2368.
[11] S. Jiang, T. Lu, J. Chen, Ab initio study the effects of Si and Mg dopants on point defects and Y diffusion in YAG, Comput. Mater. Sci. 69 (2013) 261–266.
[12] J. Li, C. Wang, X. Wang, L. Bi, Sintering aids for proton-conducting oxides – a double-edged sword? A mini review, Electrochem. Commun. 112 (2020) 106672.
[13] M. Kermani, C. Hu, S. Grasso, From pit fire to Ultrafast High-temperature Sintering (UHS): A review on ultrarapid consolidation, Ceram. Int. 49 (3) (2023) 4017–4029.
[14] K. Lu, Sintering of nanoceramics, Int. Mater. Rev. 53 (1) (2008) 21–38.
[15] E.A. Olevsky, D.V. Dudina. Field-Assisted Sintering, 1 ed., Springer International Publishing, Cham, Switzerland, 2018.
[16] B. Jia, Q. Li, L. Ma, M. Li, Y. Zhong, Z. Duan, Magnetic field-assisted sintering of nickel-doped silver microwire to improve densification and conductivity, J. Magn. Magn. Mater. 513 (2020) 167232.
[17] M. Cologna, B. Rashkova, R. Raj, Flash sintering of nanograin zirconia in <5 s at 850°C, J. Am. Ceram. Soc. 93 (11) (2010) 3556–3559.
[18] X. Hao, Y. Liu, Z. Wang, J. Qiao, K. Sun, A novel sintering method to obtain fully dense gadolinia doped ceria by applying a direct current, J. Power Sources 210 (2012) 86–91.
[19] K. Rajeswari, U.S. Hareesh, R. Subasri, D. Chakravarty, R. Johnson, Comparative evaluation of spark plasma (SPS), microwave (MWS),two stage sintering (TSS) and conventional sintering (CRH) on the densification and micro structural evolution of fully stabilized zirconia ceramics, Sci. Sinter. 42 (3) (2010) 259–267.
[20] K. Rajeswari, M.B. Suresh, D. Chakravarty, D. Das, R. Johnson, Effect of nano-grain size on the ionic conductivity of spark plasma sintered 8YSZ electrolyte, Int. J. Hydrog. Energy 37 (1) (2012) 511–517.
[21] S. Grasso, T. Saunders, H. Porwal, B. Milsom, A. Tudball, M. Reece, Flash spark plasma sintering (FSPS) of α and β SiC, J. Am. Ceram. Soc. 99 (5) (2016) 1534–1543.
[22] S. Wang, T.P. Mishra, Y. Deng, L. Balice, A. Kaletsch, M. Bram, C. Broeckmann, Electric current-assisted sintering of 8YSZ: a comparative study of ultrafast high-temperature sintering and flash sintering, Adv. Eng. Mater. 25 (18) (2023) 2300145.
[23] M. Ghatee, M.H. Shariat, J.T.S. Irvine, Investigation of electrical and mechanical properties of 3YSZ/8YSZ composite electrolytes, Solid State Ion. 180 (1) (2009) 57–62.
[24] C. Kim, I. Jang, Comprehensive review and future perspectives: 3D printing technology for all types of solid oxide cells, J. Phys. Energy 6 (3) (2024) 032003.
[25] N. Kostretsova, A. Pesce, S. Anelli, M. Nuñez, A. Morata, F. Smeacetto, M. Torrell, A. Tarancón, Single-step fully 3D printed and co-sintered solid oxide fuel cells, J. Mater. Chem. A 12 (34) (2024) 22960–22970.
[26] A. Pesce, A. Hornés, M. Núñez, A. Morata, M. Torrell, A. Tarancón, 3D printing the next generation of enhanced solid oxide fuel and electrolysis cells, J. Mater. Chem. A 8 (33) (2020) 16926–16932.
[27] A.M. Martos, S. Márquez, R.S. Pavlov, W. Zambelli, S. Anelli, M. Nuñez, L. Bernadet, J.J. Brey, M. Torrell, A. Tarancón, 3D printing of reversible solid oxide cell stacks for efficient hydrogen production and power generation, J. Power Sources 609 (2024) 234704.
[28] A. Tarancon, V. Esposito. 3D Printing for Energy Applications, Wiley-American Ceramic Society, 2021.
[29] M. Lira, N. Kostretsova, I. Babeli, L. Bernadet, S. Marquez, A. Morata, M. Torrell, A. Tarancón, Large-area 3D printed electrolyte-supported reversible solid oxide cells, Electrochim. Acta 467 (2023) 143074.
[30] K. Jia, L. Zheng, W. Liu, J. Zhang, F. Yu, X. Meng, C. Li, J. Sunarso, N. Yang, A new and simple way to prepare monolithic solid oxide fuel cell stack by stereolithography 3D printing technology using 8 mol% yttria stabilized zirconia photocurable slurry, J. Eur. Ceram. Soc. 42 (10) (2022) 4275–4285.
[31] L. Wei, J. Zhang, F. Yu, W. Zhang, X. Meng, N. Yang, S. Liu, A novel fabrication of yttria-stabilized-zirconia dense electrolyte for solid oxide fuel cells by 3D printing technique, Int. J. Hydrog. Energy 44 (12) (2019) 6182–6191.
[32] I.M. Peláez-Tirado, J.R. Marín-Rueda, J.M. Ramos-Fajardo, J.F. Valera Jiménez, M. Castro-García, J.C. Pérez-Flores, J. Canales-Vázquez, Fused filament fabrication and characterisation of 3- and 8-YSZ-based SOFC electrolytes, J. Eur. Ceram. Soc. 44 (8) (2024) 5031–5040.
[33] F. Zuo, Q. Wang, Z.-Q. Yan, M. Kermani, S. Grasso, G.-L. Nie, B.-B. Jiang, F.-P. He, H.-T. Lin, L.-G. Wang, Upscaling Ultrafast high-temperature sintering (UHS) to consolidate large-sized and complex-shaped ceramics, Scr. Mater. 221 (2022) 114973.
[34] S. Bhandari, C. Manière, F. Sedona, E. De Bona, V.M. Sglavo, P. Colombo, L. Fambri, M. Biesuz, G. Franchin, Ultra-rapid debinding and sintering of additively manufactured ceramics by ultrafast high-temperature sintering, J. Eur. Ceram. Soc. 44 (1) (2024) 328–340.

[35] T. Grippi, E. Torresani, A.L. Maximenko, E.A. Olevsky, Additive manufacturing-assisted sintering: low pressure, low temperature spark plasma sintering of tungsten carbide complex shapes, Ceram. Int. 50 (19, Part C) (2024) 37228–37240.
[36] H. Curto, A. Thuault, F. Jean, M. Violier, V. Dupont, J.-C. Hornez, A. Leriche, Coupling additive manufacturing and microwave sintering: a fast processing route of alumina ceramics, J. Eur. Ceram. Soc. 40 (7) (2020) 2548–2554.
[37] X. Zeng, C.S. Sipaut, N.M. Ismail, Y. Liu, Yy Farm, B. Peng, J. He, Preparation of 3D printed silicon nitride bioceramics by microwave sintering, Sci. Rep. 14 (1) (2024) 15825.
[38] S. Bhandari, T. Heim, E. De Bona, V.M. Sglavo, W. Rheinheimer, M. Biesuz, G. Franchin, Rapid processing of Al2O3 ceramics by fused filament fabrication and ultrafast high-temperature debinding and sintering, J. Alloy. Compd. 1017 (2025) 178812.
[39] S. Bhandari, O. Hanzel, M. Kermani, V.M. Sglavo, M. Biesuz, G. Franchin, Rapid debinding and sintering of alumina ceramics fabricated by direct ink writing, J. Eur. Ceram. Soc. 45 (5) (2025) 117144.
[40] M. Biesuz, L. Karacasulu, C. Vakifahmetoglu, V.M. Sglavo, On the temperature measurement during ultrafast high-temperature sintering (UHS): shall we trust metal-shielded thermocouples? J. Eur. Ceram. Soc. 44 (5) (2024) 3479–3485.
[41] S. Márquez, S. Anelli, M. Nuñez, M. Lira, A. Maria Asensio, M. Torrell, A. Tarancón, 3D printed electrolyte-supported solid oxide cells based on Ytterbium-doped scandia-stabilized zirconia, J. Phys. Energy 6 (1) (2024) 015016.
[42] L. Bernadet, F. Buzi, F. Baiutti, J. Segura-Ruiz, J. Dolado, D. Montinaro, M. Torrell, A. Morata, A. Tarancón, Thickness effect of thin-film barrier layers for enhanced long-term operation of solid oxide fuel cells, APL Energy 1 (3) (2023) 036101.
[43] M. Morales, A. Pesce, A. Slodczyk, M. Torrell, P. Piccardo, D. Montinaro, A. Tarancón, A. Morata, Enhanced performance of Gadolinia-doped ceria diffusion barrier layers fabricated by pulsed laser deposition for large-area solid oxide fuel cells, ACS Appl. Energy Mater. 1 (5) (2018) 1955–1964.
[44] A. Dutta, J. Mukhopadhyay, R.N. Basu, Combustion synthesis and characterization of LSCF-based materials as cathode of intermediate temperature solid oxide fuel cells, J. Eur. Ceram. Soc. 29 (10) (2009) 2003–2011.
[45] K. Matsui, H. Yoshida, Y. Ikuhara, Grain-boundary structure and microstructure development mechanism in 2–8mol% yttria-stabilized zirconia polycrystals, Acta Mater. 56 (6) (2008) 1315–1325.
[46] Z. Guo, R.I. Todd, Acceleration of grain boundary diffusion during ultra-fast firing (UHS) of alumina powder compacts, Acta Mater. 282 (2025) 120471.
[47] M. Biesuz, T.Hd Beauvoir, E. De Bona, M. Cassetta, C. Manière, V.M. Sglavo, C. Estournès, Ultrafast high-temperature sintering (UHS) vs. conventional sintering of 3YSZ: microstructure and properties, J. Eur. Ceram. Soc. 44 (7) (2024) 4741–4750.
[48] W. Ji, B. Parker, S. Falco, J.Y. Zhang, Z.Y. Fu, R.I. Todd, Ultra-fast firing: effect of heating rate on sintering of 3YSZ, with and without an electric field, J. Eur. Ceram. Soc. 37 (6) (2017) 2547–2551.
[49] M.C. Martin, M.L. Mecartney, Grain boundary ionic conductivity of yttrium stabilized zirconia as a function of silica content and grain size, Solid State Ion. 161 (1) (2003) 67–79.
[50] J.B. Goodenough, Oxide-ion electrolytes, Annu. Rev. Mater. Res. 33 (2003) (2003) 91–128.
[51] A. Weber, E. Ivers-Tiffée, Materials and concepts for solid oxide fuel cells (SOFCs) in stationary and mobile applications, J. Power Sources 127 (1) (2004) 273–283.
[52] C. Zhang, C.-J. Li, G. Zhang, X.-J. Ning, C.-X. Li, H. Liao, C. Coddet, Ionic conductivity and its temperature dependence of atmospheric plasma-sprayed yttria stabilized zirconia electrolyte, Mater. Sci. Eng. B 137 (1) (2007) 24–30.
[53] C. Ahamer, A.K. Opitz, G.M. Rupp, J. Fleig, Revisiting the temperature dependent ionic conductivity of Yttria Stabilized Zirconia (YSZ), J. Electrochem. Soc. 164 (7) (2017) F790.